Line Spectroscopy of SN2014J

Linienspektroskopie von SN2014J

Alkifron Spyridon Christodoulou

Bachelor Thesis
Physik-Department
Technische Universität München

Supervisors:	Prof. Roland Diehl
	Thomas Siegert, M.Sc.
Date of submission:	August 08, 2016

Max Planck Institute for extraterrestrial Physics
Department of High Energy Astronomy

2015

Aknowledgements

I would very much like to thank my supervisor M.Sc. Thomas Siegert for his fundamental help and care throughout the 4 months of this work. He managed in a small time window to navigate me succesfully through the steps of the data evaluation, present and explain many aspects of the nuclear astrophysics needed for getting a general overview about this field of physics.

I would also like to thank Prof. Roland Diehl for offering me this thesis and for every piece of advice and knowledge I got from him. I am really grateful to him for the encouragement throughout the project and for all the fruitful and informative meetings he arranged for me.

Munich, July 18 2015

Alkifron Spyridon Christodoulou

Contents

Symbols and Abbreviations

Symbols

I_{sp}	Specific impulse [s]
$\dot{m}$	Mass flow rate [kg/s]
F	Thrust [N]
g_0	Gravity acceleration $\left[\mathrm{m/s^2}\right]$
τ_e	Confinement time [s]
W	Volumetric plasma energy $\left[\mathrm{J/m^3}\right]$
P_{loss}	Volumetric plasma energy loss rate $\left[\mathrm{W/m^3}\right]$
n	Plasma number density $\left[\mathrm{m^{-3}}\right]$
k_B	Boltzmann's constant [J/K]
T	Temperature [K]
σ	Reaction cross section $\left[\mathrm{m^2}\right]$
v	Velocity magnitude [m/s]
$\boldsymbol{v}$	Velocity vector [m/s]
E_{ch}	Energy of reaction products [J]
G	Fusion energy gain [−]
E_{fusion}	Power produced in fusion [W]
E_{heat}	External power input [W]
η_{nozzle}	Efficiency of nozzle [−]
ρ	Density $\left[\mathrm{kg/m^3}\right]$
v_x	Velocity along x direction [m/s]
v_y	Velocity along y direction [m/s]
V	Volume $\left[\mathrm{m^3}\right]$
U	Vector of conservative variables
$\boldsymbol{F}^a$	Advection flux
$\tilde{\mathcal{E}}$	Total volume specific energy of fluid $\left[\mathrm{J/m^3}\right]$
$\tilde{\mathcal{E}}_T$	Thermodynamic volume specific energy of fluid $\left[\mathrm{J/m^3}\right]$

$\tilde{\mathcal{E}}_K$	Kinetic volume specific energy of fluid $\left[\mathrm{J/m^3}\right]$
$\tilde{\mathcal{E}}_M$	Magnetic volume specific energy of fluid $\left[\mathrm{J/m^3}\right]$
$\tilde{\mathcal{E}}_{in}$	Perturbation energy of fluid $\left[\mathrm{J/m^3}\right]$
$\boldsymbol{B}$	Magnetic field vector [T]
$\boldsymbol{B}_0$	External magnetic field vector [T]
$\boldsymbol{B}_{in}$	Induced magnetic field vector [T]
p	Thermodynamic pressure $\left[\mathrm{N/m^2}\right]$
$\tilde{p}$	Sum of thermodynamic and magnetic pressure $\left[\mathrm{N/m^2}\right]$
$\tilde{p}_{in}$	Perturbation pressure $\left[\mathrm{N/m^2}\right]$
γ	Heat capacity ratio [−]
μ_0	Magnetic permeability constant [H/m]
S	External sources
$\underline{\underline{\boldsymbol{I}}}$	Identity tensor [−]
$\boldsymbol{j}$	Current density $\left[\mathrm{A/m^2}\right]$
v_S	Speed of sound [m/s]
v_A	Alfven speed [m/s]
v_M	Magnetosonic speed [m/s]
v_ϕ	Phase velocity [m/s]
$\boldsymbol{k}$	Wave vector $\left[\mathrm{m^{-1}}\right]$
$\boldsymbol{e}_n$	Normal unit vector [−]
$\boldsymbol{e}_t$	Tangential unit vector [−]
s	Coordinate along curved field line [m]
R	Radius of curvature of field line [m]
ω	Wave angular frequency $\left[\mathrm{s^{-1}}\right]$
θ	Angle [deg]
A	Area $\left[\mathrm{m^2}\right]$
$\boldsymbol{n}$	Surface normal vector [−]
λ_{max}	Highest wave speed [m/s]
Δx	Spatial increment [m]
r_p	Plasma initial radius [m]
R_c	Coil radius [m]
I	Coil current [A]
Z	Atomic number [−]

q	Ion charge [C]
m	Plasma mass [kg]
M	Molar mass [kg/mol]
R_{gas}	Gas constant [J/(mol · K)]
N	Number of ions [−]
$\bar{v}$	Average ion speed [m/s]
Ma	Gas dynamic Mach number [−]

Abbreviations

1D, 2D, 3D	one, two, three dimensions / -dimensional
ICF	Intertial Confinement Fusion
NIF	National Ignition Facility
IEC	Inertial Electrostatic Confinement
MTF	Magnetized Target Fusion
VISTA	Vehicle for Interplanetary Transport Applications
NASA	National Aeronautics and Space Administration
MHD	Magnetohydrodynamics
PIC	Particle In Cell
SPH	Smoothed Particle Hydrodynamics
PDE	Partial Differential Equation
ODE	Ordinary Differential Equation
FVM	Finite Volume Method
LF	Lax-Friedrichs
UHV	Ultra High Vacuum

Abstract

The goal of this thesis is to study SN2014 and search for possible produced positrons. These should emerge during the decay of ^{56}Co. Using a post-explosion time window of almost 5 months, data from a gamma-ray telescope called INTEGRAL has been analysed, after applying a background model developed for this purpose.

A possible positron detection in SN2014 can provide further information about the production sites of this anti-particle and can lead to further investigation on this area. For example, a goal of future works can be calculating the fraction of positrons found in the center of the galaxy coming exclusively from Type Ia supernovae.

1. Introduction

On the 21th of January 2014 S.J Fossey and four undergraduate English students in London noticed a bright star in the neighbouring Galaxy Messier82 they did not expect to see. Comparing the new images with archival images proved that this 'new star' was actually a supernova, which got baptized 'SN2014J', as it was already the 10th supernova spotted in this year.
The shortly after obtained early spectra classified this supernova, which is located at a distance of 11.5 ± 0.8 light-years (3.5 ± 0.3 Mpc), as a Type Ia supernova. The closest for more than 40 years!

A major product of explosive nucleosynthesis in type Ia supernova explosions is ^{56}Ni. This radioactive isotope, with a relatively short half-life of 8.8 days decays to ^{56}Co. The cobalt-isotope has a half-life of 111.3 days and can decay (with a 19% probability) via β^+-decay to ^{56}Fe. A β^+-decay takes place when a ~~positron~~-rich nuclei converts a proton into a neutron. In order to keep the charge in balance, a positron e^+ is emitted.

A positron is ~~according to the standard model~~ the antiparticle of an electron. Both leptons share the same rest mass of 511kev, but differ in the charge, since electrons are negative charged and positrons are positive charged particles.

Positrons, which are produced during the β^+-channel of Cobalt decay, collide inelastically inside the supernova ejecta cloud lose their kinetic energy and form an bound state with electrons, called the **positronium**.

A positronium is similar to a hydrogen atom. Instead of having the heavy proton as the positive counterpart, a positronium has an positron forming an exotic atom. This bound state is quite unstable and annihilates in less than one nanosecond to produce two or three gamma-ray photons, depending on the relative spin of the particles. The positron and the electron combine for a total mass energy of 1022kev, two times 511kev. Thus, the photons produced from the annihilation share 1022kev and if only two gamma-ray photons are produced, each of them carries an energy of 511keV.

Since the news, that a supernova in the neighbourhood has illuminated the sky, have been spread, most astronomic observations tools on earth and in orbit, including INTEGRAL (Interantional Gamma Ray Astrophysics Laboratory), turned their telescope towards this rare celestial event. INTEGRAL is an ESA satellite operating since 2002. Despite it been initially planned to operate till 2007, it is still orbiting our earth nowadays, providing the astrophysical society with data. This satellite carries two major instruments on board, including a gamma-ray spectrometer, called **SPI**, which measures high energy photons in an energy range of a few keV up to 20MeV, producing a wide gamma-ray energy spectrum.

Due to the fact that gamma-ray spectrometers are ~~enormously~~ background-dominated, a very accurate **background model** has to be developed, in order to distinguish the celestial sources from the background. The main idea behind it lies in the use of spectral information and detector properties over time.

The main goal of this thesis is to investigate the supernovae's spectrum, then understand and eventually use the background model and finally detect the 511-keV line, which correlates with the positron yield in the supernova.

Chapter 2 discusses the evolution and explosion of type Ia Supernovae and takes a closer look into SN2014 discussing its characteristics, abnormalities and assumptions. The high energetic gamma-rays, their production methods, sites and the way they interact with matter are discussed in chapter 3. In chapter 4, a short overview of ESA's satellite, INTEGRAL, as well as its observing spectrometer, SPI, is given. The background model used for getting the actual SN2014J spectrum is discussed in chapter 5. Chapter 6 presents the data evaluation results and the discussion and finally, chapter 7 summarizes the thesis and discusses the results of chapter 6.

.

2. Stellar Explosions

2.1. Type Ia supernovae

Type-Ia supernovae are generally understood to result from binary systems consisting of one carbon-oxygen white dwarf and a companion, with a wide range of different properties. The matter accreting from the companion to the white dwarf causes the latter to reach a stability mass limit, the so called **Chandrasekhar mass**, which is around $1.44M_{\odot}$, ultimately exceed it and ignite carbon fusion located in the centre of the white dwarf. This ignition in the degenerate matter inside the white dwarf releases large amounts of energy, enough to overcome the binding energy of it and leads to the thermonuclear runaway.

2.1.1. General Properties

The most easy way to distinguish type Ia supernova explosions from other types of explosions, e.g. type II supernova, is the absence of hydrogen absorptions lines. In addition to that, most of type Ia supernovae show a remarkable similarity, of ~~it it~~ ~~has been~~ taken advantage for many years.

In Supernovae's early optical spectra intermediate mass element-lines of Si, Ca, Mg, S and O can be found, indicating their presence in the outer layers of the ejecta. Iron-group element lines are initially absent, since the SN Ia remains opaque for several days. However, within several weeks, more and more from the ^{56}Ni lines, powering the light curve can be detected. Due to the fact that ^{56}Ni has a short half-life before decaying to ^{56}Co, it is actually ^{56}Co that maximizes the light curve 70-100 days after the explosion. Afterwards, the intensity of the light-curve declines, as ^{56}Co, with a half-life of 108.8 days, decays.

In terms of nucleosynthesis, its is general consensus that type Ia supernovae are the major production sites for ^{56}Ni and therefore for most of the iron-group elements. Typical ^{56}Ni masses extracted from bolometric light curves are between $0.3M_{\odot}$ and $0.9M_{\odot}$. Typically, a Type Ia supernova produces

around $0.5M_{\odot}$ of ^{56}Ni. Ten times more than a core-collapse supernova does.

2.1.2. Progenitor Models

Type Ia supernovae have always played an important role in astrophysics. For many years their relative homogeneity made them usable as distance indicators for cosmology and for determining the expansion history of the Universe. However, more recent observations showed diverging properties among them. Hence, the simple model of a Chandrasekhar-mass white dwarf exploding must get upgraded with more progenitor scenarios, in order to explain this diversity in the explosions.

Nevertheless, the progenitor system of SNe type Ia remains a unsolved problem. It is safe to say that these explosions happen due to thermonuclear explsions of white dwarfs, mostly consisting of carbon and oxygen. As said before, white dwarfs are ~~unconditionally~~ stable, so only an interaction with another star may ~~force~~ them to explode.

Throughout the years, two major binary progenitor systems have been established. On the one hand the traditional **single-denerate progenitor system**, composing a white dwarf and a main-sequence supergiant star. On the other hand the novel **double degenerate scenario** with the merge of two white dwarfs.

The single-degenerate scenario (SD) contains a white dwarf and a main-sequence supergiant star. The latter transfers matter, mostly its hydrogen envelope, in a stable manner to the companion, increasing its mass, density and temperature. When the critical conditions, for carbon-burning, have been achieved, the energy getting ~~freed~~ leads to a thermonuclear explosion, destroying the white dwarf entirely and blowing the companion star away.
Some alternations of this scenario have been developed as well, including a 'Helium-donator' instead of a 'hydrogen-donator' or a so called **double detonation**-scenario, which suggests that it is not necessary for the white dwarf to reach the Chandrasekhar-mass to explode. The main idea behind it lies in a early detonation in the helium-layer that may detonate under the right physical conditions, which leads to a second detonation inside the white dwarf and thus to the actual SN Ia explosion.

The other leading progenitor scenario is the double degenerate (DD) scenario.

In this case two ~~carbon-oxygen~~ white dwarfs merge and exceed the Chandrasekhar limit. This scenario matches very well with theoretical birth rate calculations, population-synthesis models and is able to explain the SN Ia rates. The main idea behind the merge of two white dwarfs lies in the oscillating mass transfer from one white dwarf to the other, depending on which has the higher mass. At last, a common envelope is evolved and the merger is unavoidable. However, the double degenerate scenario has received a lot of criticism, as many scientists doubt the likelihood of this kind of thermonuclear explosion or e.g. the production of sufficient ^{56}Ni. Other assume that this kind of mass accretion would cause outer layer burning and maybe to a transformation into an oxygen-neon-magnesium white dwarf instead of a thermonuclear explosion.

2.1.3. White dwarfs

A **white dwarf** refers to a compact stellar remnant composed of electron-degenerate matter. These compact objects with a mass similar to the mass of the sun and a volume comparable to that of the earth are the most common final stage in the evolution of stars. Characteristically, all stars which are not massive enough ($\leq 8\ M_{\odot}$) to explode via type II supernovae and form either neutron-stars or black holes, form white dwarfs.

Depending on the initial mass of a low or medium mass main-sequence star, a star reaches its last burning stage, which can either be the hydrogen burning, for very low mass stars, helium burning, carbon burning and oxygen burning for more massive ones or even neon burning. This last burning product piles up in the centre of the star, but the local densities and temperatures are not high enough to start the fusion of it. When it has consumed all of its fuel, the star loses its last source of energy ~~and only force~~ to counter the gravitational force, sheds its outer layers and starts contracting under its own weight. At last the contraction stops as electrons become degenerate at very high densities ($\rho = 10^6 \frac{g}{cm^3}$).

The result of this contraction is a very stable and dense stellar remnant, called **white dwarf**. Most white dwarfs are composed of carbon and oxygen. Nevertheless also helium white dwarfs and oxygen-neon-magnesium dwarfs may form.

Despite them been the final stage of low mass stars and not being able to fuse further elements, white dwarfs still undergo evolution. At the very begin of their 'life' they have high luminosities, but in the course of several million

years they cool down and fade away into invisibility.

White dwarfs are in general stable objects. However, if accompanied by a binary companion, like a main-sequence star, matter can accrete from the companion star to the white dwarf and increase the mass of it.
If a certain critical mass, the Chandrasekhar mass with around $1.44 M_{\odot}$ is reached, the density and the temperature in the centre of the white dwarf become so high, that the previously unfused element in the center of it -mostly carbon- starts fusing. This fusion reactions ignited inside the degenerate matter of such a dense object releases large amounts of energy, enough to overcome the binding energy of it and thus causes a supernova explosion, which is classified as the type Ia supernova explosion.

2.1.4. Type II supernovae

Massive stars over $\sim 8 M_{\odot}$ do not form white dwarfs, but may explode and leave neutron-stars or black-hole behind, as a supernova remnant.

These stars are massive enough to go through all burning stages and start piling up iron in their core. Iron, is the element with the highest binding energy and thus the most stable element, as it can not produce energy by fusing. The iron core in the centre of the star remains initially stable by the electron degeneracy pressure. If however a critical mass, which can be associated with the Chandrasekhar-mass of the white dwarfs, but depends on the electron fraction in the core Y_e, is reached, the iron core implodes, causing the outer layers to collapse towards the center of the star. This produces peak temperatures of 100 billion Kelvin and causes the Iron elements to photodisintegrate into free protons and neutrons forming a so called **Proton-neutron star PNS**. At last, the collapse is halted by the neutron degeneracy pressure and bounces back ~~towards outwards~~. Pushing the collapsing outer layers to the opposite directions causes the shock to lose its energy and thus it finally stalls.

~~In the last years theories~~(~~e.g.Woosley et al.2002, Sukhbold et al. 2016~~) suggested that inside the proton-neutron star, neutrinos are being produced, while protons convert to neutrons by β^+-decay. If these high energy neutrinos deposit a fraction of their kinetic energy to the stalled shock, the latter may revive and lead to the successful explosion of the star, which is classified as a type-II supernova or called 'core-collapse' supernovae.

Nevertheless, not all of the massive stars are able to explode. Stellar collapses that fail to create a strong outwoard moving shock may implode and form black holes. Black holes can also be created in successful explosions that experience a large amount of fallback.

Depending on several characteristics of the progenitor star, like rotation, initial mass, final mass cut etc, either a neutron-star, a very massive compact object consisting of neutrons, or a black hole will be left behind as a stellar remnant. Observations (Özel & Freire 2016) constrain the gravitational mass of a neutron star between $1.0M_{\odot}$ and $1.8M_{\odot}$ and ~~this~~ of a black hole $5M_{\odot}$ and $20M_{\odot}$ (Wiktorowicz 2014).
~~(In the formulation described in Eq. ??)~~

2.2. SN2014J

As mentioned before SN2014J was discovered on January 22,2014 in the nearby starburst galaxy M~~ossey~~82 (Fossey et al.2014) at a distance of 3.5 Mpc and with galactic coordinates (l,b)=(141.427°, 40.558°). It was ~~immediately~~ classified as a type Ia supernova. Zheng et al. (2014) calculated the explosion date as the 14 January, UT 14.75. The brightness of the ^{56}Ni lines indicates, that about $0.5M_{\odot}$ were produced, which is a very characteristic value for type Ia supernovae. In many ways it appears to be a 'standard' type Ia supernova.

Nonetheless, Diehl et al. (2014) observed some **abnormalities** concerning the timing in which ^{56}Ni-lines were observed. This abnormalities may lead to major ~~refinements to~~ the current supernova type Ia models.
To become more specific, INTEGRAL, the International Gamma-ray Astrophysics Laboratory started observing SN2014J on 31 January 2014, 16.6 days after the inferred explosion date. It would be to late to search for ^{56}Ni on the surface of the ejecta, where it is generally believed to be less abundant than deep in the expanding supernova cloud. Integral data however, clearly show the characteristic nickel decay lines at 158keV and 812keV, which indicate, that a rather significant ammount, close to 10% of the total mas, of ^{56}Ni was located near the surface.

Due to this fact, ~~novel~~ progenitor scenarios have been hypothesised. A merger of two white dwarfs could possibly explain the observation of ^{56}Ni in the outer layers of the supernova. The most favorable scenario, according to Diehl et

al. (2014), speaks of an 'explosion that might have been triggered by a surface helium explosion from a helium belt that has built up rapidly from matter accreted from the companion star'. This scenario differs from the classical single degenerate scenario, since the donator star transfers helium to the white dwarf instead of hydrogen. Thus, the progenitor system of SN2014J can be imagined as a intermediate between a white dwarf and a main-sequence star binary (single degenerate) and two white dwarfs (double degenerate). This scenario fits well with the population synthesis models for a starburst galaxy like M82. A double detonation explosion scenario can be ruled out, as it would produce broad gamma-ray emission lines, which was not the case for SN2014, as narrow lines have been detected.

3. Gamma rays

Gamma rays are a form of high-energy electromagnetic radiation consisting of high-energy photons. They were discovered in the beginning of the 20^{th} century by the French chemist Paul Villard, who studied the radiation of Radium. As a matter of fact, he observed the radiation coming from the de-excitation of Radium from a high energy state to a lower energy state. Ernest Rutherford, who discovered himself alpha and beta rays, named these forms of electromagnetic radiation gamma rays.

Nowadays, gamma rays are a key tool for studying and understanding nuclear astrophysics. Their advantage is that they trace nuclear processes directly, as gamma-rays originate from nuclear decays, de-excitation and high-energy collisions.
Comparing gamma-rays with other forms of radiation (Radio, IR, opt, UV), gamma rays differ only in the order of magnitude of their energy, since they are the most energetic form of radiation known till today. They cover a big part of the energy spectrum ranging from a few keV to TeV.

3.1. Gamma ray production

Generally, gamma rays can be produced by a large variety of phenomena, both nuclear and non-nuclear.

3.1.1. Radioactive decay (gamma decay)

A radioactive decay is probably the most common production mechanism of gamma rays. This form of decay takes place when an excited nucleus decays to a lower energy state, emitting a gamma ray photon of the respective energy. It usually occurs after an α- or a β-decay, since both leave the nucleus mostly in an excited state. Other possibilities that can trigger a gamma decay are neutron capture, electron capture, a nuclear fusion or a nuclear fission.

A characteristic example for a radioactive decay is the beta-decay of ^{60}Co to excited ^{60}Ni, which then decays to the ground state by emitting gamma rays. To become more specific, unstable ^{60}Co decays via β^--decay to an excited state of ^{60}Ni (J^π=4+). In less than a picosecond, and with a probability of 99.88%, the excited nucleus decays to the ground state by emitting ~~back to back~~ photons of 1.17 MeV and 1.33 MeV. The number of photons emitted depends on the nucleus and reveals that a series of nuclear energy levels exist.

3.1.2. Matter-antimatter annihilation

Another important gamma ray source, which also plays a fundamental role in this bachelor thesis, is the matter annihilation. According to the Standard Model in particle physics, every particle has a respective antiparticle.
For instance, the antiparticle of a proton, is called 'anti-proton' with the same rest mass like its antiparticle, but a opposite charge of the same order.
Also electrons, the most common negative leptons, have positive antiparticles of the same mass, called **positrons**.
A matter annihilation takes place when a particle and its anti-particle collide and annihilate in two, or three photons. These photons share an energy equivalent to the rest masses of the particles that annihilated.
In the case of the positron-electron pair there are more than one path that leads to the annihilation. They can either annihilate immediately and produce two photons, each carrying an energy ammount of 511keV, or they can build an unstable exotic atom, called the **positronium**. In this bound state, an electron and a positron orbit around their common centre of mass.

A positronium, like the hydrogen atom, has two possible configurations of its ground state, depending on the relative orientations of the spins of the particles, called the **para-positronium** and the **ortho-positronium**.

The para-positronium is the singlet state (S=0, M_s=0), where the particles have antiparallel spins. It decays mostly within 125 picoseconds in an even number of photons, preferably into two.

The more ~~durable~~ ortho-positronium , is the triplet state (S=1, M_s=-1,0,1), as both particles have parallel spins. This configuration has a mean lifetime of 142 nanoseconds and decays into an uneven number of photons, preferably into three, dividing its energy onto them and producing tje ortho-positronium-continuum.

Combining all three variations of the electron-positron-annihilation, a characteristic spectrum is obtained.

3.1.3. Other production mechanisms

In addition to the radioactive decay and the matter annihilation, gamma rays can be produces by various particle-photon interactions or by particle decay. For instance, the π^0-Meson, with a rest mass of $135.0\frac{Mev}{c^2}$ can decay in two photos via the electromagnetic force. Other examples are the synchrotron radiation, which occurs when charged particles ~~in synchrotrons~~ are accelerated radially using magnetic fields and the so called 'bremsstrahlung', produced by the deceleration of charged particles ~~approaching~~ a coulomb field.

3.2. Production sites

There are many different sites, where energetic events produce gamma rays. Most of them can be found far away from our planet and its protective atmosphere, not excluding however that also our earth is a possible gamma ray producer.

A major source of gamma-rays are so called pulsars, fast rotating neutron stars with vast magnetic fields. They produce focused beams of high relativistic charged particles, which then emit gamma rays via bremsstrahlung as they are passing through gas nebula.

Also simple neutron stars are potential sources of gamma-rays. These supernova remnants accrete material from their environment, which gets excited and emits photons in the gamma-regime.
Some of the most powerful gamma-ray photons come from quasars, the center of active galactic nuclei (AGN). The radiation coming from an AGN is thought to come from the accretion of matter by supermassive black holes in the center of active galaxies. They produce charged particles into beams, which again interact with their environment (gas, dust) and produce amongst other types of radiation also gamma-ray radiation.

The most energetic, but at the same time rare, sources of gamma rays are Gamma-ray bursts (GRB). They realise vast amounts of energy in the same

order of magnitude as supernova explosions and last approximately for two seconds. It is believed that a GRB occurs, when two neutron-stars or a neutron-star and a black hole merge.

Also our Earth can host events that produce gamma radiation. For instance, terrestrial thunderstorms produce accelerating electrons which interact with the surrounding atmosphere and produce gamma rays by bremsstrahlung.
~~(In Eq. ??,)~~
~~(in the works presented in [25], [24] and [35].)~~

3.3. Interaction of Gamma-rays with matter

As mentioned before, the gamma-ray energy spectrum ranges from a few keV to TeV. Photons with such high energies are able to interact with matter i.e. with the telescopes used for detecting them. This interaction of gamma-rays with matter is welcomed, since it is the only way to detect gamma-photons. Therefore, it is important to list and summarize the three principal interactions: the photoelectric effect, the Compton effect and the pair-production.

3.3.1. Photoelectric effect

The lower edge of the gamma-ray energy range is dominated by the photoelectric effect. In this effect, an incoming photon transfers all its electromagnetic energy E_γ to ~~an~~ atomic electron and is absorbed. If the energy transferred from the photon to the electron is more than the energy needed for the electron to overcome the Coulomb potential of the atom, the electron is kicked out of it, and its kinetic energy can be calculated as the difference of the photon energy and the work function.

3.3.2. Compton effect

Photons with an energy around 500keV interact with matter via the Compton effect that dominates around these energies. The main idea behind it is the inelastic scattering of a photon by a charged particle, causing the photon to lose some energy and change its direction. The scattering angle θ depends on the energy loss of the photon, providing information about the direction of the photon.

3.3.3. Pair production

For energies higher than 1022keV (two times 511keV), the possibility of the reverse process of the matter annihilation, the pair production, is available. Pair production is the creation of an elementary particle and its respective antiparticle, usually a ~~proton and a~~ positron pair, from a photon in the presence of a charged particle. For photons at MeV scale, pair production is the dominant mode of photon interaction with matter. The presence of a nucleus is important in order to satisfy conservation of momentum.

4. INTEGRAL and SPI

In the previous chapter the production mechanisms and creation sites of gamma-radiation have been discussed. In order to understand cosmic phenomena and improve our view of the universe, it is crucial to construct telescopes that are able to detect these gamma-ray fluxes.
However, detecting gamma-rays is associated with fundamental problems. To begin with, it is impossible to detect them on Earth, due to the opaqueness of the atmosphere, absorbing most of the gamma-ray flux heading for our planet. Secondly, being so energetic, cosmic gamma-ray fluxes are very low. A cosmic event that produces a certain amount of energy needs much fewer gamma-ray photons than e.g. optical photons to transport away its produced energy.
In addition to the low gamma-ray fluxes, the high penetrable nature of gamma-rays make their collimation by mirrors impossible. Thus, the only way to observe gamma-rays is by detecting them not directly but rather indirectly by the produced particles.
Still the biggest and most fundamental problem while dealing with photons from the upper end of the electromagnetic energy scale is the domination of the **intrinsic background** in the observed spectra.

Astrophysicists have been able to bypass most of these problems. In order to dodge the opaqueness of the atmosphere, gamma-ray telescopes have been mounted on satellites, orbiting the Earth or on balloons, to avoid most of the Earth's atmosphere.
To counteract the low gamma-ray fluxes, it is necessary to built telescopes with large effective areas and let the observation times in one particular direction (pointing) be long enough ($\geq$ 30 min).
In order to distinguish the intrinsic background from the actual celestial sources, a precise background model, that can predict the background sources accurately, must be developed. The background model used for INTEGRAL and SPI is discussed in chapter 5.
Finally, as mentioned before, the detection of gamma-rays conceals difficulties. The idea of detecting these particles and the methods used are discussed in this chapter.

4.1. Detecting methods

One of the most fundamental problems of gamma-rays is that they are very penetrable. Thus, it is impossible to collimate them with mirrors. Since they can not be detected directly, this must be done indirectly by detecting the produced charged particles.
In modern high energy spectroscopy two different detector types are preferred, scintillation detectors and semiconductor (solid-state) detectors.

4.1.1. Scintillation detectors

Scintillation detectors is one opportunity to detect gamma-rays. They can be subdivided in organic and inorganic detectors, depending on the material the scintillator is made of.
The main idea behind a scintillation detector is the following: When a high energy photon meets a scintillator, an organic or inorganic material, it excites an electron from the valence band into the conduction band. Depending on the material used as a scintillator, this electron will return to the valence band producing a low energy photon.
In order to produce photons in the energy range of visible light and make the recombination more probable, the initially pure scintillator is doped. Scintillation photons produce a weak signal and must therefore be transferred into a detectable electronic signal using photomultiplier tubes (PMT) or avalanche photodiodes (APD).
Photomultiplier tubes are able to multiply the signal produced by scintillation photons enough to become easily detectable by e.g. oscilloscopes. PMTs used for detection of gamma rays consist of a photocathode, where the incident photons strike and produce, via the photoelectric effect, free electrons. They are navigated toward various electrodes, called dynodes, were more electrons are freed. After passing many dynodes a large number of electrons reaches the negative charged anode producing a easily detectable sharp current pulse.
A second option for multiplying a weak signal are avalanche photodiodes. APDs are superconductors modified by applying a reverse bias. By this way, incoming photons gain on the way to the cathode more kinetic energy, enough to free further electrons that do they same and cause an electron avalanche easily detectable.
Scintillation detectors have fast response times but relatively low energy resolution, due to the large band gap. Organic scintillators also bear a low density that makes them not suitable as gamma-ray detectors, since an interaction with

gamma-rays becomes improbable. On the other hand, inorganic scintillators have fast response times, making them suitable as anticoincidence shields. In order to achieve high energy resolutions for gamma-ray spectroscopy, though, **semiconductor detectors** are the first option of gamma telescope manufactures.

4.1.2. Semiconductror (Solid state) detectors

The main idea behind semiconductor detectors is to place a semiconductor material, like Germanium or Silicon, between two electrodes, an anode and a cathode.

Incoming gamma-ray photons interact with the semiconductor by setting electrons free and thereby creating holes. The number of free electrons and created holes is proportional to the energy of the incoming photon, the more energetic the photon, the more electrons it frees. Electrons and holes travel toward the electrodes creating a weak signal. In order to strengthen this signal a reverse bias has to be applied. This can happen simply by implanting Lithium at the inner surface of the detector, producing a n-type diode.

Semiconductor detectors are much denser than scintillation detectors. Besides, they are relatively small and have fast response times making them suitable for gamma-ray detection. In addition, their smaller band gap (Germanium has e.g. a band gap of 0.67eV at room temperature, whereas scintillators one of several eV) leads to a higher probability of excitations and recombinations and therefore to a better energy resolution. On the other hand, such a small band gap requires a cooling system, since even at room temperature electron-hole pairs can be built by thermal excitation.
Choosing the right combination of detectors for building and protecting the instruments of INTEGRAL requires therefore careful consideration. The actually used detector types are discussed bellow.

4.2. The INTEGRAL mission

INTEGRAL (International Gamma Ray Astrophysics Laboratory), the telescope designed for fine spectroscopy and imaging of celestial gamma-ray emission sources (Winkler et al.2013), was launched on the 17^{th} of October 2002 from Baikonur/Kazakhstan.

The European Space Agency (ESA) designed this mission as a follow-up mission for the Compton Gamma Ray Observatory (CGRO), that would last for maximum 5 years. Surprisingly, INTEGRAL still orbits the Earth and continues to deliver gamma-ray data till today.
INTEGRAL carries four coaligned instruments on board, two major telescopes, SPI and IBIS, and two rather complimentary instruments, OMC and JEM-X. Most of them are using the **coded mask system**.

4.2.1. Coded mask system

The main idea behind a coded mask system, is to place a mask, consisting of several transparent and opaque blocks, in front of the detector array. These blocks create a known shadow pattern on the detectors. By doing so, some detectors are completely overshadowed, some are partly overshadowed and some not overshadowed at all. Changing slightly the viewing position of the satellite causes the shadow pattern to cast its shadow on different detectors. Using complex computer-based deconvolution algorithms (Caroli et al. 1987), it is thereby possible to determine the location of the source.
Coded-mask systems have a wide 'fully coded field of view' (FCFV). This is defined as comprising all directions for which the recorded flux is completely modulated by the mask. The 'partially coded field of view' (PCFV) on the other hand is defined as 'comprising al the directions for which only a fraction of the detected flux is coded by the mask' (Caroli et al. 1987).
The coded mask system has turned out to be a very successful tool for determining the location of the incoming photons, and was therefore used in every instrument on INTEGRAL lacking a spatial resolution.

4.2.2. INTEGRALS' instruments

Spectrometer SPI, the high spectral resolution gamma-ray telescope of INTEGRAL, is able to detect photons with an energy between 20keV and 8MeV. It consists of 19 high purity Germanium detectors and in order to provide spatial information about the incoming photons it operates in conjunction with a coded-mask system. Since SPI is the only instrument used for the data evaluation, a more detailed description of its function can be found in the next subsection.
Imager IBIS on the other hand is a Compton telescope and observes gamma-rays in the energy range between 15keV and 10MeV. It uses a coded-mask-system like SPI to gain information about the direction of the photons and

consists of two layers of detector arrays. IBIS uses a larger number of less massive detectors than SPI in order to provide a better spatial resolution (12 arcmin), but lacks high energy resolution ($\sim$ 10 %). Being a telescope with high spatial resolution and decent energy resolution, it focuses more on point sources, complementing by this way SPI, which focuses more on exact energy values.
The Joint European X-Ray Monitor (JEM-X) is one of the complementary instruments installed on INTEGRAL. It is a X-ray monitor with an angular resolution of 3 arcmin, an effective area of 500cm^2 and a FCFV of 10°. It consists of two coaligned telescopes, both with an individual coded mask, recording spectra in the energy range between 3 and 35keV.
The second complementary instrument on INTEGRAL is the Optical Monitoring Camera (OMC), a classical camera observing the optical emission for the same sources the other instruments focus on.

4.2.3. Orbit

The orbit of INTEGRAL had to be chosen very carefully in order to avoid the radiation damage caused by the **Van Allen radiation belt**. This belt consists of two main regions with intense radiation that is held around the Earth due to Earth's magnetic field.
The inner Van Allen belt is located 1.000-6.000km above the earth and contains high concentrations of energetic protons and electrons, trapped by its strong magnetic fields.
The outer Van Allen belt contains mostly high energy electrons and is found at altitudes between 13.000km and 60.000 km. It has been observed, that its width and particle density can fluctuate, depending on the activity of the Sun.
In order to avoid the damage that these radiation belts can cause to all instruments mounted on INTEGRAL, a highly eccentric orbit with an inclination of 52.5° to Earth's rotational axis has been chosen.
With a perigee height of only 9.000km and the apogee height almost 154.000km, it takes 3 days for the satellite to orbit the Earth.
Since this orbit cannot avoid the radiation belts completely, INTEGRAL's observation hold on for a specific time, while the satellite is located near the earth.
To be more specific, scientific observations start at an altitude of 40.000km leaving the Van Allen radiation belts and stop at 60.000km approaching them, losing only 10% of observation time.

Generally, the performance tests of INTEGRAL lasted approximately nine months after launch. Only after assuring that the satellite works reasonably, did the satellite start delivering data.

4.3. SPI

4.3.1. Main detector array

As mentioned previously, INTEGRAL's spectrometer SPI is the only instrument used for the data evaluation. Since it has been designed for fine gamma-ray spectroscopy, a solid state detector type has been chosen. This consists of 19 high purity Germanium (HPGe) detectors ordered in a hexagonal structure, covering a geometrical area of 508cm^2 and is able to detect photons with an energy between 20keV and 8MeV. In order to create a detectable signal, the detector array has been placed on an Aluminium capsule and a high-voltage of 4kV across the detectors has been chosen, transferring the initially pure Germanium blocks into reverse-biased n-type diodes. The spectral resolution of them is between 2.5keV and 3keV, depending on the energy bin.

Like most of the instruments on INTEGRAL, SPI operates in conjunction with a coded-mask system, placed 1.71m above the detector array. The coded mask consists of 127 hexagonal elements accumulating a diameter of 720mm, providing a FCFV of 16° and a PCFV of 31°. 63 elements, made of thick tungsten, are opaque for gamma-rays and 64 let them through. A coded-mask with 127 'pixels' in conjunction with a detector array containing 19 Germanium detectors ('pixels') with the aforementioned dimensions result a spatial resolution of 2.5°.

4.3.2. Anticoincidence systems

As previously stated, background lines and continuum dominate the energy spectrum in the gamma-ray regime.
Nevertheless, there have been several efforts to reduce it and therefore several different background-reducing components have been installed on SPI.
The most important one is the heavy hexagonal anticoincidence shield (ACS). It is made of 91 bismuth germanate (chemical formula: $Bi_4(GeO_4)_3$) crystals surrounding SPI from almost every direction, yielding an additional mass of 512kg to the satellite. As it is made of an inorganic scintillator (BGO), astrophysicists can rely on its fast response times in order to trigger a veto signal,

every time a photon comes from the wrong direction.
The anticoincidence shield managed to reduce the background by a factor of 25 (Jean et al.,2003), creating however some additional unavoidable BGO background lines.

4.3.3. Cooling system

The relatively small band gap of Germanium (0.67 ev at room temperature) provides on the one hand many benefits and requires on the other hand special treatment, since it is much easier to create electron-hole pairs by thermal excitation.
For this reason, the detector array must be permanently cooled down to approx. 90K. The cooling system of SPI, contains four Stirling machines located inside a beryllium shell, called the Cold Box. Despite, using once again background reducing precautions, the Cold Box is contributing significantly with its own characteristic lines to the background spectrum.

4.3.4. After launch observations

INTEGRAL was launched on the 17^{th} of October 2002 from Baikonur/Kazakhstan and it took nine months of performance tests and other kinds of checks, like the determination of the imaging response function, to begin recording celestial data.
As expected, cosmic radiation and the passage through the Van Allen radiation belt caused serious damage on the detectors, worsening their resolution dramatically. Luckily, this has been awaited and in consequence, SPI has been programmed to heat its detectors twice a year to 105°C, purging them of all defects caused by cosmic radiation or possible micrometeorites.
Unfortunately, four detectors have received irrevocable damage during various perigee passages and ceased recording data. For this reason, detector 2, failed in December 2003, detector 17 in July 2004, detector 5 in September 2009 and detector 1 in May 2010 have not been used in the data evaluation of this thesis.

5. Instrumental Background

A fiducial parameter, which is present when taking gamma-ray data with telescopes situated far away from Earth's protective atmosphere, is the high intrinsic background.
Cosmic rays hit gamma-ray telescopes orbiting the earth, ~~like~~ INTEGRAL, ionize and excite every material on it and produce unwanted gamma-ray photons. Almost every material on INTEGRAL is a potential background source: the solar cells, cables, background shields, other instruments, even the detectors themselves.
As discussed before, background photons outweigh celestial photons by a factor which is very close to 100. For this reason, gamma-ray astronomers need to develop background models in order to to 'filter' it out and ~~re~~tain the actual celestial spectrum.
This bachelor thesis used an already available background model for INTEGRAL, called **spimodfit**, developed many years ago, lastly modified in 2014 by Siegert and will investigate the dependence of the data in respect to the time, sun activity, detector location e.t.c.

5.1. What is a background model?

The task of a background model is to estimate precisely the number of background photons for every energy range, detector and pointing, without counting in sky photons. In order to separate mathematically these photons, the following formula is needed:

$$D_{ijk} = \sum_{m,n} R_{ijk}^{mn} \sum_{s}^{N_S} \alpha_s S_s^{mn} + \sum_{t} \sum_{b}^{N_B} \beta_{b,t} B_{b,ijk} \tag{5.1}$$

Equation 5.1 distinguishes cosmic photons from background photons. D_{ijk} describes the photon counts in one energy bin i, one certain detector j and one pointing k. It contains photons from both sources. The first part of the sum refers to celestial counts and the second part to background counts. S_s^{mn} are

the sky sources, $B_{b,ijk}$ the background sources and R_{ijk}^{mn} refers to the instrumental response function. Since only celestial photons pass through the coded mask system and cast a shadow on the detector array, the response function is relevant only for them. The sums over the celestial and background sources indicate that several of these sources are present. In the following subsections it will be proved that the background is time/revolution-dependent, thus the background sources require a summation over the time. The galactic longitude and latitude are thereby described with the indices m and n respectively. Finally, parameters α_s and $\beta_{b,t}$ describe the intensity of their respective type of source. They are obtained after fitting an expected background model and an expected sky model to the measured counts. Especially α_s is of vital importance, since it describes the intensity of a celestial source. Before fitting a model to the data though, it must be decided, which data is meaningful and which must be rejected.

5.2. Factors that influence the spectra

First of all, it is important to filter raw data and leave out data that looks unpromising. For example, even though INTEGRAL observations stop when approaching the Van Allen radiation belts, it has been proved that they still influence the events rate. For this reason the program 'spimodfit' reduces further the observing time, by filtering out data recorded in the proximity of the radiation belt. In addition to this, the following chapter discusses how natural cosmic influences, like the activity of the Sun and the effects on its environment, affect the spectra. Finally, it is important to note the time-dependence of the detectors degradation.
All this parameters have to be taken into account in order to keep merely useful data, which can be used for data evaluation.

5.2.1. Solar flares

A factor that causes ~~trouble to~~ INTEGRAL's instruments are solar flares. Solar flares are sudden flashes of light on the surface of the Sun, emitting great amounts of energy. It is believed that solar flares occur, when a phenomenon called 'magnetic recollection' takes place. The Sun's surface contains numerous loops of magnetic lines, always connected with the Sun. If such ~~a line escapes~~ the Sun's surface, it releases a great amount of energy and charged particles forming a coronal mass ejection. These charged particles hit INTEGRAL and mostly interact with the protective shields of SPI, like the anti-coincidence

shield (ACS). Still, these solar flares are a potential candidate for additional background and therefore data recorded during a solar flare must be excluded.

5.2.2. Solar Cycle

The solar activity is a term that describes the behaviour of the Sun, considering the strength of solar radiation, ejection of mass, number of sunspots, solar flares and others. Throughout the centuries it has been observed that this activity follows a characteristic periodic cycle. To be more specific, it has been observed that solar cycles last approximately 11 years, within them the solar activity reaches a minimum and a maximum.
While dealing with data from INTEGRAL, the solar cycle must be studied and analysed as a indirect potential source of additional background photons.
For instance, when the solar activity reaches its maximum, the Sun produces a stronger magnetic field protecting its surroundings - and thereby the Earth along with the other inner planets and INTEGRAL - from cosmic flux. This causes the count rates of both the protective shields and the detectors to go down. On the other hand, when the Sun activity is around its minimum, like in the end of 2009, INTEGRAL is exposed to a higher cosmic flux, causing the detectors to measure a higher background.

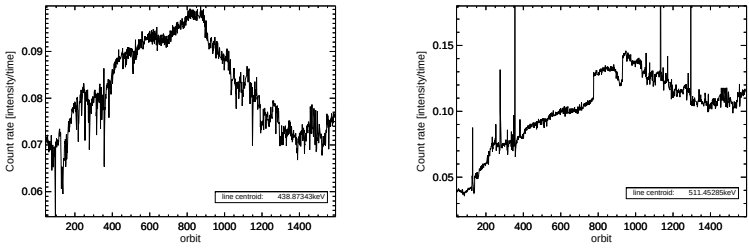

Figure 5.1.: Count rate per revolution

Figure 5.1a,b prove the anti-correlation of the detector count rate for the 438keV- and the positron-line with the solar activity. INTEGRAL was launched in 2002, as the Sun's activity was close to its maximum. Figure 21a,b shows

characteristically, that around revolution 850, which refers to the end of the year 2009, the count rate reached a maximum, as the Sun went through a very quiet phase. While this thesis is written, the Sun just passed a solar maximum and starts calming down. Thus, it is expected that in the following revolutions the count rate will start rising again.

5.2.3. Detector Degradation

As mentioned before, the pure crystalline structure of the Germanium detectors gets damaged through cosmic radiation, causing a detector degradation. This degradation affects the spectra and especially spectral lines. Instead of ideal gauss-shaped lines SPI starts representing them in combination with an exponential tail function, causing a spectral line to have a higher Fully Width Half Maximum (FWHM) over time. This can be seen in the following plot:

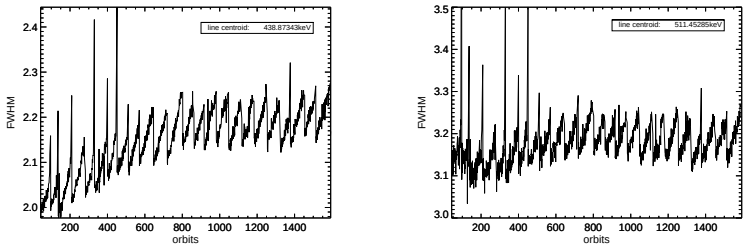

Figure 5.2.: FWHM per revolution

Figure 5.2a,b shows the FWHM of the 438keV-line and the positron-line per orbit. The FWHM is a way to observe the energy resolution and degradation of the Germanium detectors through the revolutions. It is noticeable that the energy resolution worsens, until it is restored back to an acceptable value. This process, called **'Annealing'**, takes places twice a year, where the detectors are heated to approx. 105 °C in order to purge the structure of the detectors. Of course, even after Annealings, it is impossible to fix the detectors completely, so a trend towards higher FWHM and thereby worse energy resolution is visible throughout the years. Even here, one might state, that a sun activity pattern

can be suggested, as since approx. revolution 800 the degradation has remained constant or even gives way. This suggestion can be confirmed in the following years, if the overall degradation starts rising again.

5.3. Background models for INTEGRAL

There have been several different approaches to build a background model for INTEGRAL. A very gross estimate is to observe an area with no celestial sources, for example for latitudes $b > \pm 30^{\circ}$. By this way, it is possible to identify lines coming from background sources. However, in the previous subsections it has been proved that the background sources change from revolution to revolution and in addition to this, the photon counts show a great variation even from pointing to pointing. For this reason, it is inconsistent to use this fairly simple idea to predict the background counts.
A fairly good background model was developed by Wang et al. in 2007. and used independent measurements of different instrumental parameters. In a matter of fact, they used PSAC(plastic scintillator anti-coincidence shield, designed to reduce the background around the 511keV line) rate for predicting the background around a specific energy range. Despite some successes of this background models, it has been suggested that it over-fits the spectra and therefore it is also fitting noise.

5.3.1. Current background model

The most recent and in the same time accurate background model of INTEGRAL was developed by Thomas Siegert in 2014. It exploits spectral information in broad energy regions, information about long-term detector response change and bases on two major hypotheses. First, the relative intensities of the detectors (=¿ detector ratios) are constant for one epoch. Second, the spectral lines do not vary from pointing to pointing but rather from revolution to revolution.
In other words, detectors always measure the same intensity in respect to other detectors, as long as the number of functioning detectors stay the same. If a detector gets destroyed, this ratio has to be determined once more. In addition, background counts do not change significantly within one revolution, since the detector degradation/damage takes mostly place while passing the Earth's radiation belts.

This bachelor thesis will investigate the properties of detector ratios and discuss whether they can contribute in distinguishing pure background sources from lines that include a celestial signal. In addition, it will be analysed how detector pattern can help locating background sources on the INTEGRAL spacecraft.

5.3.2. Detector Ratios

Detector ratios are defined as the relative intensity of one detector in respect to all the other detectors. This relative intensity can originate either from a line, the continuum of a specific energy range or the total spectrum.
Ideally, without any background contribution, this ratio should only depend on the shadow of the coded mask and on the direction of the celestial sources, which would cause some detectors to measure photons and some not. Since the whole satellite produces background photons, all detectors measure photons, which do not depend on the coded mask system. It can even be suggested, that the majority of background sources emit very homogeneous radiation, thus every detector should measure roughly the same intensity.

Siegert(2014) calculated the total intensity of the 450-640keV region and found out that this is true. The total intensity depends primarily on the weight of every detector. What happens however if individual spectral lines are studied? Siegert showed that the relative intensities for single spectral lines deviate significantly from the average and followed interesting patterns.
Is it hence possible to dig out a celestial signal from such background dominated data? The main ideas of using detector ratios to analyse the background are the following:

To begin with, it is possible to use detector ratios to suggest possible background sources and their location in the spacecraft. For example, if the inner detectors 1-6 have a higher relative intensity in respect to the outer detectors, it can suggested that a background source is situated very near to the detector array. As a matter of fact, Siegert showed that the 1779keV ^{28}Al-line has a higher relative intensity for inner detectors in respect to the outer detectors, which can be easily explained, as the Germanium detectors are mounted on Aluminium capsules.
On the other side, the opposite can be argued for the 1764keV line of radioactive Bismuth coming from the anti-coincidence shield (ACS). In this case it is hypothesised that the outer detectors should measure a higher intensity in respect to the inner detectors.

This bachelor thesis calculated the relative intensities in the 3^{rd} epoch (after losing detector 2 and 17) for four different lines, 438keV, 511keV, 570keV and 574keV. The lines are approximated by a Gaussian function with four parameters.

$$G(E) = A_0 exp(-\frac{(E - E_0)^2}{2\sigma^2}) \tag{5.2}$$

A_0 is the amplitude of the line, E_0 the energy corresponding to the peak of the line, σ^2 is variance, a parameter describing the width of the line and τ which is not used in this formula, symbolizes an exponential tail function, due to the fact that the degradation of the detectors moves lines towards lower energies. This factor complicates the formula and is not needed for calculating the intensity of the line. In order to do that, a simple formula is needed.

$$I(A_0, \sigma) = \sqrt{2\pi} A_0 \sigma \tag{5.3}$$

Using equation 5.3, which is actually the integral over the whole energy range of the line, it is possible to calculate the intensity of a line.

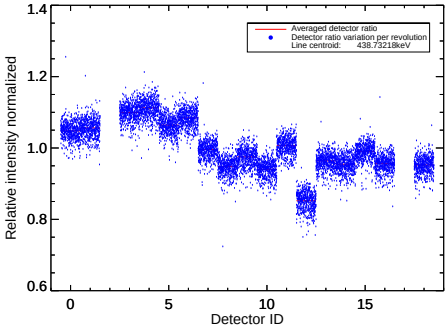

Figure 5.3.: Detector ratios for the 438keV-line

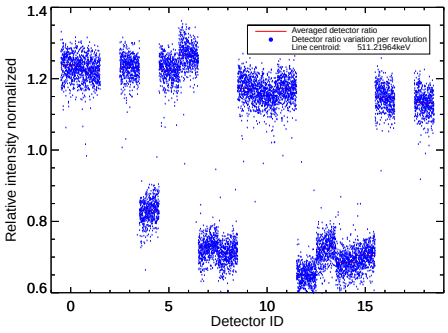

Figure 5.4.: Detector ratios for the positron-line

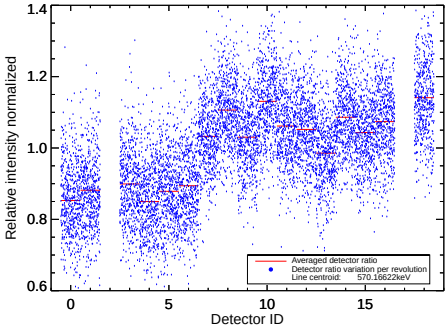

Figure 5.5.: Detector ratios for the 570keV-line

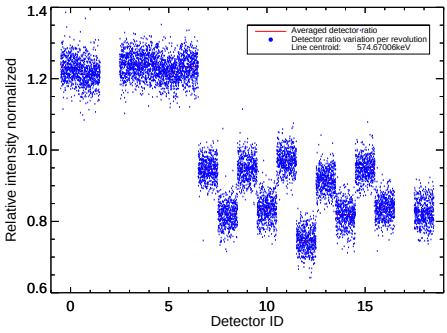

Figure 5.6.: Detector ratios for the 574keV-line

Figures 5.3-5.6 present the detector ratios for the three most significant lines of the energy range between 420keV and 620keV. These are 438keV-, 511keV- and 574keV- and the smaller 570keV-line. The horizontal red line stands for the averaged detector ratio and the small blue lines show this intensity in the course of the revolutions of the 3^{rd} epoch, building a smaller time-scale on the red line.

For the 438keV and 574keV lines the inner detectors 1-6 have a higher relative intensity in respect to the outer detectors, indicating a background source coming from the detector array itself. The very low deviation of the relative intensities confirm the assumption that instrumental lines variate little during one epoch. For the 574keV line, there is even a difference between detectors located at the edge of the detector array 7,9,11,13,15 and the ones located at the corners 8,10,12,14,16,18.

The positron line does not show a symmetric pattern. It can be suggested, that adjacent detectors mostly measure the same intensity and that some detectors located at the left side of the camera, as seen in figure 121 all measure a lower intensity. Still the reasons for this specific pattern are questionable.

The 570keV line is a less intensive line and therefore the variation per revolution is higher. However, this case is showed, since the detector ratios follow the opposite pattern of the detector ratios for 438 and 578keV. In this case, the

outer detectors 7-18 have a higher relative intensity indicating a background source coming from the ACS shield or another material that encompasses the detector array.
Instrumental lines, especially the most dominant, change only slightly in the time scale of one epoch. If such a line shows a higher variation per revolution, it can indicate a possible celestial signal.

6. Results

The primary goal of this thesis is to detect the positron 511keV line in the SN2014, by applying the background model discussed in the previous section. For the data evaluation the energy spectrum between 420keV and 630keV was used. This does not look promising in a first look, since it is entirely background dominated [6].

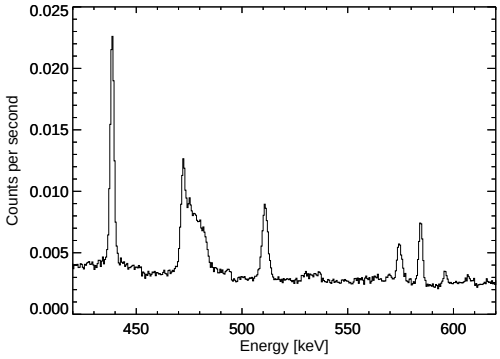

Figure 6.1.: Counts per second for the energy range between 420keV and 630keV for the entire INTEGRAL mission

Figure 6.1 shows the counts per second for the entire INTEGRAL mission. It contains five very dominant lines, three of them, the 438keV, 511keV and 574keV-lines, discussed as detector ratio-examples. Due to the background domination of the data, the background model discussed in the previous section, must be used to obtain the actual celestial signal.

Before doing so, the adequacy of the background model must be tested on an already known and multiple times observed sky source, e.g. the 'Crab'. If the results match well with literature values, it indicates a compatible background model that can be used for the SN2014J data evaluation.

6.1. The 'Crab'

The Crab Nebula is a supernova remnant, located at a distance of approx. 2kpc in the constellation of Taurus. It was first observed by early Chinese astronomers in 1054 and nowadays it is believed to belong to the low energy branch of core-collapse supernovae (Nomoto et al. 1982). In the center of the nebula a pulsar, a fast rotating neutron star, can be found. The Crab Nebula has been studied, observed and modelled multiple times by various astronomers and telescopes. Even INTEGRAL and SPI observes it regularly and its data has been analysed by various observing teams (Jourdain et al. 2009). This bachelorthesis used data from four early revolutions, 43-46, in order to ~~constitute~~ its spectrum.
The gamma ray energy spectrum of the Crab Nebula (galactic coordinates: l = 184.6°, b = 5.8°) can be described by a powerlaw function:

$$f(E) = AE^k \tag{6.1}$$

This indicates, that the Crab Nebula spectrum in the gamma ray regime can be described precisely by two parameters.
Figures 6.2a,b plot the gamma-ray spectrum between 422keV and 630keV of the Crab Nebula. The left plot is the original spectrum with the counts per second per surface area for every energy bin of 0.5keV. The right plot sums up 424 energy bins of 0.5keV in only 8 energy bins of 53keV in order to receive a clearer spectrum and reduce the error bars in the flux. In both plots the tendency to a powerlaw function is perceptible.
Fitting the spectrum with IDL's procedure **curvefit** delivered values for both parameters. Since the parameters depend on the initial guess, one parameter has been fixed to a value suggested by Jourdain et al 2009 and finally both variations have been compared with the values of Jourdain et al 2009.

Comparing the two fits with the literature values provided by Jourdain et al. (2009), it is clear that there ~~roughly~~ no difference between them. Most data points are in a distance of one σ within the literature values. This indicates

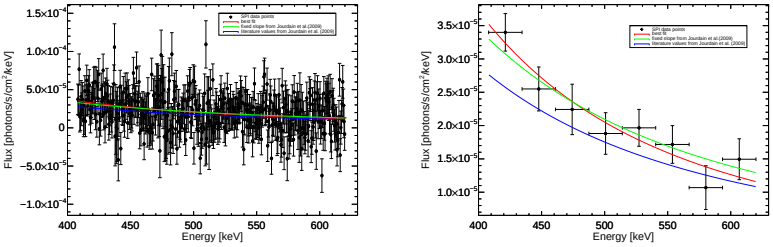

Figure 6.2.: Gamma ray spectrum of the Crab Nebula with two different rebinning factors

Table 6.1.: Crab Nebula Parameters

Parameters	A	k
best fit (red)	$A = 2.05^{-5} \pm 1.12^{-6}$	$k = -2.66 \pm 0.43$
fixed slope (green)	$A = 2.09^{-5} \pm 1.02^{-6}$	$k = -2.24 \pm 0.00$
literature values (blue)	$A = 6.45^{-4} \pm 0.00$	$k = -2.24 \pm 0.00$

that the background model applied works well and can be used for the study of SN2014J.

6.2. SN2014J

Since the background model is able to describe satisfactorily the Crab Nebula, ~~it~~ was applied for the SN2014J. INTEGRAL observed it from revolution 1380 till revolution 1428. SN2014J is located in the M82 galaxy at the galactic coordinates l=141° and b=40°. Inserting the ~~correct~~ data into **spimodfit** produces the following spectra.

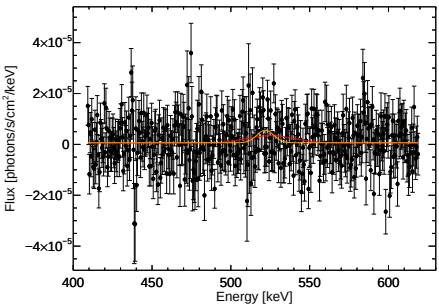

Figure 6.3.: Gamma ray spectrum of SN2014J, energy bins: 0.5keV

Figure 6.3 presents the actual spectrum for the entire observing time window. It does not look promising at the beginning, due to the scattering of the counts. However, if single energy bins are summed up, a clear positron signal can be seen. Figures 6.4, 6.5 and 6.5 present the same plot as figure 6.3 with different rebinning factors.
The spectrum has been described by a constant line C, representing the continuum and a Gaussian function in the position of the positron line:

$$p(E) = C + Aexp(-\frac{(E-E_0)^2}{2\sigma^2}) \tag{6.2}$$

In the same way as for the crab, the final fit depends on the initial guesses given for the parameters. The red slope portraits the best fit for parameters thought to be suitable to the spectrum.

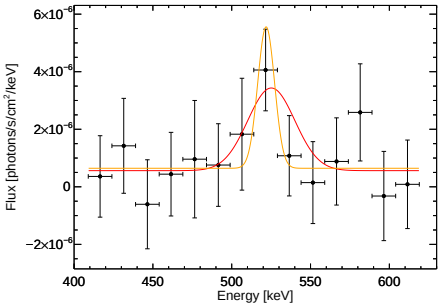

Figure 6.4.: Gamma ray spectrum of SN2014J, energy bins: 15keV

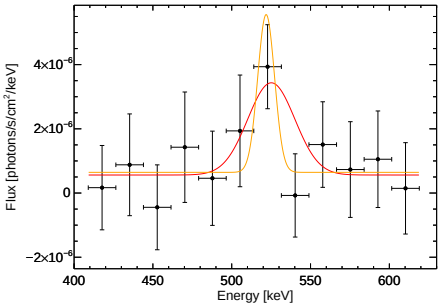

Figure 6.5.: Gamma ray spectrum of SN2014J, energy bins: 17.5keV

For the orange ~~slope~~, parameter σ has been set to a fixed value, using information about the spread velocity of ^{56}Co. As discussed in a previous chapter, ^{56}Co is the direct producer of positrons. Since it is moving out, it causes a

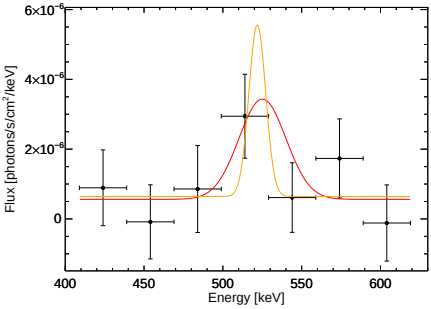

Figure 6.6.: Gamma ray spectrum of SN2014J, energy bins: 30keV

broadening of the positron line, known as Doppler broadening. The ~~breadth~~ of the positron line, FWHM, proportional to σ, depends therefore on the spread velocity of Cobalt and on the energy resolution of the instrument, SPI (equation 6.3). Using the spread velocity of Cobalt in a time window between 66.3 and 99.1 days after the explosion from Diehl et al. (2014) and with the following formulas, a fixed σ can be set.

$$v = \frac{c}{E_0}\sqrt{FWHM_{source} - FWHM_{resolution}} \tag{6.3}$$

$$FWHM_{source} = 2\sqrt{2ln2}\sigma \tag{6.4}$$

Inserting for E_0=511keV, for c the speed of light and 2.5keV as SPI's energy resolution, results for σ_{source}:

$$\sigma_{source} = 5.33 \tag{6.5}$$

For the orange fit, this value has been inserted as a fixed parameter.
As can be seen in table 6.2, fixing a certain parameter influences the other parameters, as well as the errors.

Nonetheless, both fits deliver similar results. As an indicator of the quality of the fit, χ^2-test can be carried out.

Table 6.2.: SN Parameters

Parameters	C	A	E_0	σ
red fit	$5.62 \cdot 10^{-7}$	$2.87 \cdot 10^{-6}$	525.11	14.94
σ_{redfit}	$\pm 4.27 \cdot 10^{-7}$	$\pm 1.89 \cdot 10^{-6}$	± 9.12	± 8.76
orange fit	$6.44 \cdot 10^{-7}$	$4.91 \cdot 10^{-6}$	521.84	5.33
$\sigma_{orangefit}$	$\pm 4.24 \cdot 10^{-7}$	$\pm 1.90 \cdot 10^{-6}$	± 3.25	± 0.00

χ^2 is actually understood as the difference between the model used for fitting and the actual data:

$$\chi^2 = \sum_i \frac{(D_i - M_i)^2}{\sigma^2} \tag{6.6}$$

The χ-square-test for the red fit delivers 444.8, while the for the orange fit 441.6, showing that both fits are almost equally suitable.

Table 6.3.: fitproperties

Parameters	χ^2	total line intensity
red fit	444.8	$1,08 \cdot 10^{-4} \pm 9.49 \cdot 10^{-5}$
orange fit	441.6	$6.56 \cdot 10^{-5} \pm 2.54 \cdot 10^{-5}$

Table 6.3 shows, that although both fits are almost equally good, reducing σ to a fixed value has an impact on the total line intensity. In this case, the intensity was reduced by 40%.

6.3. Line flux

The last task was to calculate the line flux, first for the entire observing time and then for four different periods, the same chosen by Diehl et al. (2014), in order to determine the creation time of the positrons and see how well it correlates with the line flux of ^{56}Co. (Fig.4 on their paper). In addition, the

line flux was compared with three different explosion models, discussed and analysed in The et al. (2014).

6.3.1. SN2014 explosion models

The et al (2014) modelled explosions with 15 different explosion models for this supernova.(reference) Three of them seem to fit well with the observations of SN2014J and will be compared with the positron line flux calculated in this thesis:

W7 (Nomoto, Thielemann, Yokio (1984), a standard Type Ia explosion model that includes deflagrations and has explosions properties typical for type Ia SNe. **hed8** (Hoeflich et al. 1996), a sub-Chandrasekhar helium detonation explosion model, that is favoured by Diehl et al., as it fits well with their observations and finally a pulsating delayed detonation explosion model **pdd54**, developed by Hoeflich et al. (1995). This model uses slow deflagration to induce pulsation before detonation.

The characteristics of these explosion models can be viewed in the following table 6.4:

Table 6.4.: Explosion model Characteristics

Model	Total Mass in $M_\odot$	^{56}Ni Mass in $M_\odot$	Explosion Energy in 10^{51}erg
W7	1.38	0.56	1.3
hed8	0.96	0.51	1.03
pdd54	1.38	0.17	1.02

However, it has been suggested by both my supervisor, Thomas Siegert and Prof. Roland Diehl, that The et al. (2014) overlooked a factor of 2 in their line fluxes. For this reason, the line fluxes for the three models have been multiplied by this factor.

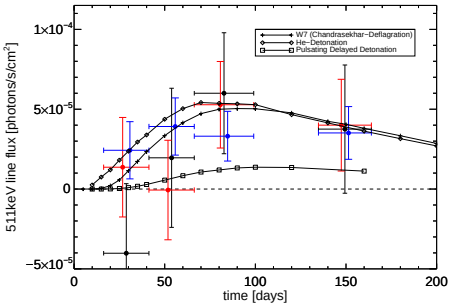

Figure 6.7.: Line flux of the positron line for four different epochs and three different fits

6.3.2. Light curve

Figure 6.9 plots the line flux of the positron line. In order to plot it like a light curve, the observations have been subdivided into four epochs of post-explosion days. The first epoch covers 16.3-41.3 days after the explosion, the second 41.3-66.3, the third 66.3-99.1 and the forth 134.8-164.0. In the last epoch the supernova should already be transparent.

As mentioned previously, all three models have been multiplied by a factor of 2. Three different fits have been used (black, red, blue). The black fit uses the parameters calculated by curvefit for the line intensity. The red fit, has a fixed $\sigma = 5.33$ like the orange fit in figures 6.3-6.6 and the blue fit has also a fixed position of the peak at $E_0 = 521.84$.

While studying figure 6.7, it becames clear that the pulsating delayed detonation model does not ~~fit~~ with the data. On the other hand, the other two models, W7, hed8, ~~fit well~~ with the line fluxes calculated and the multiplication with the factor 2 looks reasonable.
The helium detonation model, especially, suggested by Diehl et al.(2014) as a very likely progenitor model fits exceptionally well with the last two data

points. For the first two epochs, INTEGRAL could barely detect a positron signal, suggesting that the positron annihilation rate at these times was low. All three fits follow the same trend. The positron flux rises till day 90 were it reaches a maximum and then slowly starts dropping, matching well with the ^{56}Co abundances in the supernova cloud.

7. Conclusion

The purpose of this work was to simulate a fusion plasma thruster and to investigate the modeling of the physical effects when using the ideal MHD equations. Fusion thrusters make use of the kinetic energy released during fusion processes by redirecting the ion products for the generation of thrust. The potential use of fusion thrusters in future interstellar missions calls for the presence of different techniques which can be used for their simulation.

Based on existing works which utilized different physical and numerical models (PIC, hybrid, SPH), typical initialization parameters of the plasma properties can be derived. Since the processes of ignition and hydrodynamic expansion after the fusion reaction do not belong to the topic of this work, conditions with macroscopic plasma expansion are chosen as initial conditions for the simulation. For the applications considered, the plasma properties are characterized by very high speeds resulting from the fusion process.

In order to compare the simulations with literature, the plasma properties have to be modified to suit the ideal MHD model without compromising the physical integrity of the problem. However it is found that certain parameters like the charge of the ions lack sufficient modeling in the ideal MHD case and hence could alter the underlying physical principles. On the other hand, thermodynamic properties which do not require modeling in particle methods, need special treatment in the case of ideal MHD. A disadvantage of the chosen model lies in the representation of the vacuum conditions in a way that does not induce numerical instabilities but still does not affect the integral quantities.

With the modified initial conditions, results for the expansion of the plasma in the present of a constant magnetic field can be obtained. The influence of the magnetic field strength on the efficiency of the nozzle is examined and shows that an increased field strength also improves the thrust performance. Similar results yield from the examination of a coil magnetic field, where a time dependent increase in the efficiency is observed and quantified. The model of MHD also captures the movement of plasmas for a wider range of velocities

and demonstrates better results in the case of lower speeds.

Due to the fact that the plasma is modeled as a fluid, the presence of waves is unavoidable when examining solutions with a strong external magnetic field. Although these waves represent physical phenomena which are existent in plasmas satisfying the MHD assumptions, their resolution triggers numerical instabilities. Moreover, the 1st order FVM which was implemented for the calculations is the one with the highest stability due to its dissipative nature but still cannot avoid all numerical problems. It is expected that higher order schemes would lead to even higher instabilities.

It is also evident, that physical structures and regions with high magnetic field gradients like the conductor coils used in magnetic nozzles, require special treatment to moderate the solution in their vicinity. Although efforts were made to diminish these unwanted effects, no results could be obtained for the thrust performance for larger time scales.

Ideal MHD is an attractive modeling tool for plasma applications due to its relatively simple formulation. It is shown to provide qualitatively correct solutions in the case of fusion thruster modeling as far as redirecting the plasma in the magnetic nozzle is concerned. However, due to the induced complexity resulting from the wave propagation and extreme pressure rarefactions in the presence of high speeds and magnetic field strengths, its effectiveness is considered to be less than in the case of particle-based and hybrid methods.

Since most presented disadvantages are connected to numerical issues, special treatments of the strong gradients could pose a suitable solution without the need of changing the underlying physics. Another possible suggestion would be to extend the model to include viscous effects (resistive MHD) and to examine which effects can be subsided with this formulation. In general, the physical description of the problem is sufficient in the case of MHD and is able to provide results for smaller speeds and time scales, which implies that with proper treatment of the numerical issues, a complete description of variable plasma thruster configurations could be achieved.

A. 1D Simulation of velocity discontinuity

In Section 3.2, the effect of a uniform disc initialization was examined. It was mentioned that according to Toro [34], a numerical vacuum condition is obtained at the origin of the velocity discontinuity. Specifically, Toro performs a shock tube simulation with different gas dynamic conditions for the fluid at right and left parts of the domain as described in Table A.1.

Table A.1.: Initial Conditions defined in [34]

Property	Left	Right
Velocity	-0.2	0.2
Pressure	0.4	0.4
Density	1.0	1.0

The results of the simulation after 0.15 time units are shown in Fig. A.1.

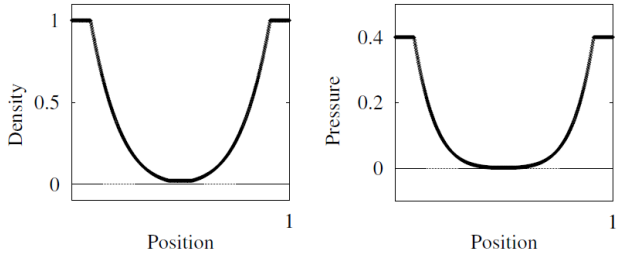

Figure A.1.: Density and pressure plots for 1-D gas dynamic shock tube simulation [34]

In order to verify the process for the values used in Section 3.2, a 1D simulation

was set up with the initialization shown in Fig. A.2

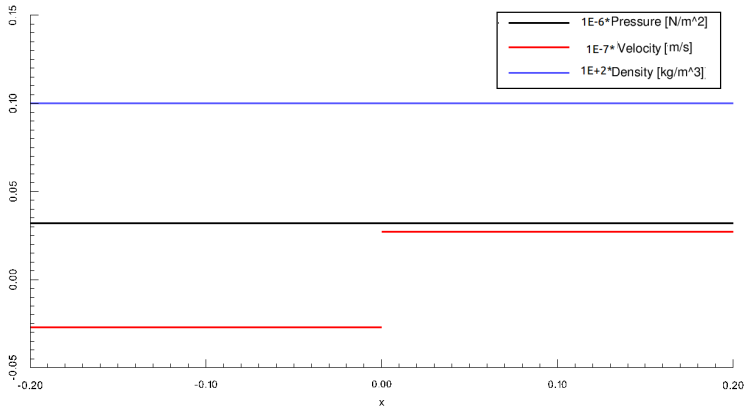

Figure A.2.: Initial conditions of the 1-D Simulation

The solution of the 1D shock tube expasion problem lead to a sharp decrease in the pressure and density as illustrated in Fig. A.3. The values of the thermodynamic properties close to the origin are close to zero and therefore the numerical issues triggered by this type of initialization are clearly demonstrated.

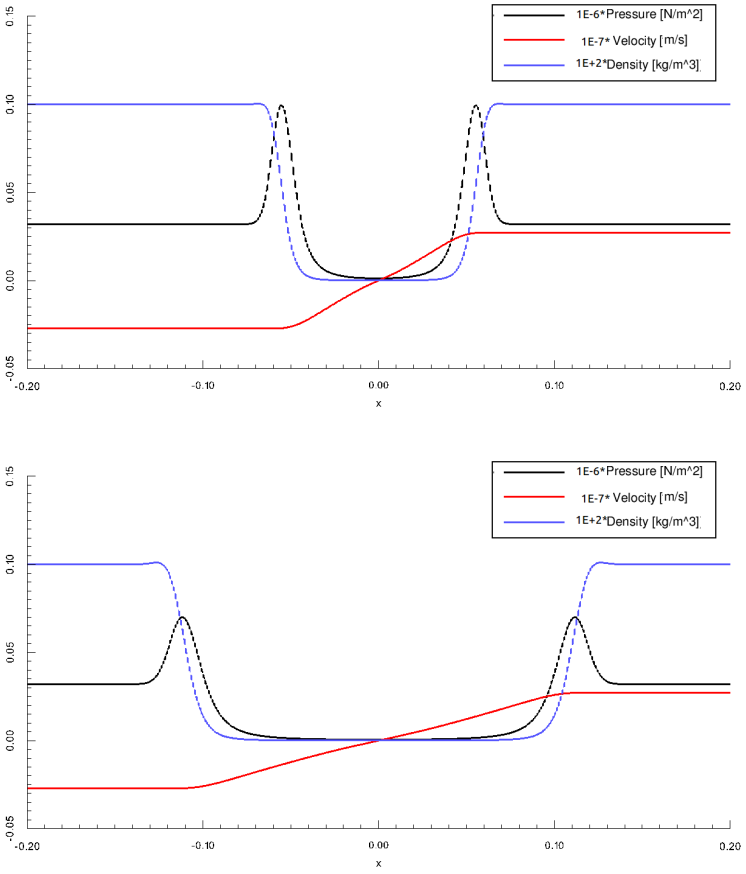

Figure A.3.: Density, pressure and velocity plots for 1D gas dynamic shock tube simulation after 2 μs and 4 μs

B. Calculation of efficiency for constant field

In Section 6.1, the efficiency of the nozzle was examined in the case of a constant magnetic field. In the case of an isotropic expansion and a uniform magnetic field, the net impulse in the x direction (the desired thrust direction) becomes zero. For that reason, only half of the domain was examined in order to quanitfy the compression that the magnetic field causes.

The net impulse in the x direction is hence positive even in the case of a uniform expansion in the absence of an external field. The value of this equivalent efficiency for the isotropic case is easily obtained by taking into account the sketch in Fig. B.1.

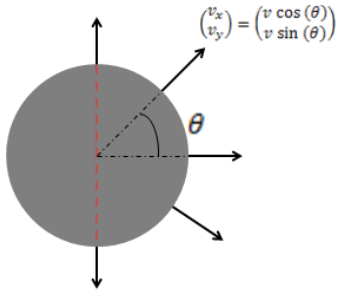

Figure B.1.: Isotropic expansion and velocity vectors

The velocity of each element can be described by the vector $(v_x, v_y)^T = (v \cdot \cos(\theta), v \cdot \sin(\theta))^T$. The magnitude of the velocity is $v = \sqrt{v_x^2 + v_y^2}$. Since only the region for $x > 0$ is of concern, θ takes values between $-\pi/2$ and $\pi/2$. The efficiency according to Eq. **??** becomes

$$\eta_{nozzle} = \frac{\int \rho v_x \, \mathrm{d}V}{\int \rho v \, \mathrm{d}V} = \frac{r^2/2 \int_{-\frac{\pi}{2}}^{\frac{\pi}{2}} \rho v \cos(\theta) \, \mathrm{d}\theta}{r^2/2 \int_{-\frac{\pi}{2}}^{\frac{\pi}{2}} \rho v \, \mathrm{d}\theta} = \frac{2}{\pi} \approx 0.63662 \tag{B.1}$$

It is therefore expected that a magnetic field along the positive x direction will always provide values for this equivalent efficiency higher than 0.63662.

C. Meshes

The domain used in the simulations consisted of a stretched mesh as shown in Fig. C.1 and Fig. C.2. The depicted mesh consists of 100 nodes in each direction whereas the mesh used throughout the simulations was made up of 800 nodes in each direction. The dimensions of the mesh were chosen to be 10x10 meters in the cases without external field. For the simulations with external magnetic field, the dimensions of the mesh were changed to 20x20 meters as explained in Section **??** and the number of elements along each direction was also doubled leading to 1600x1600, whereas the stretch parameters were kept equal.

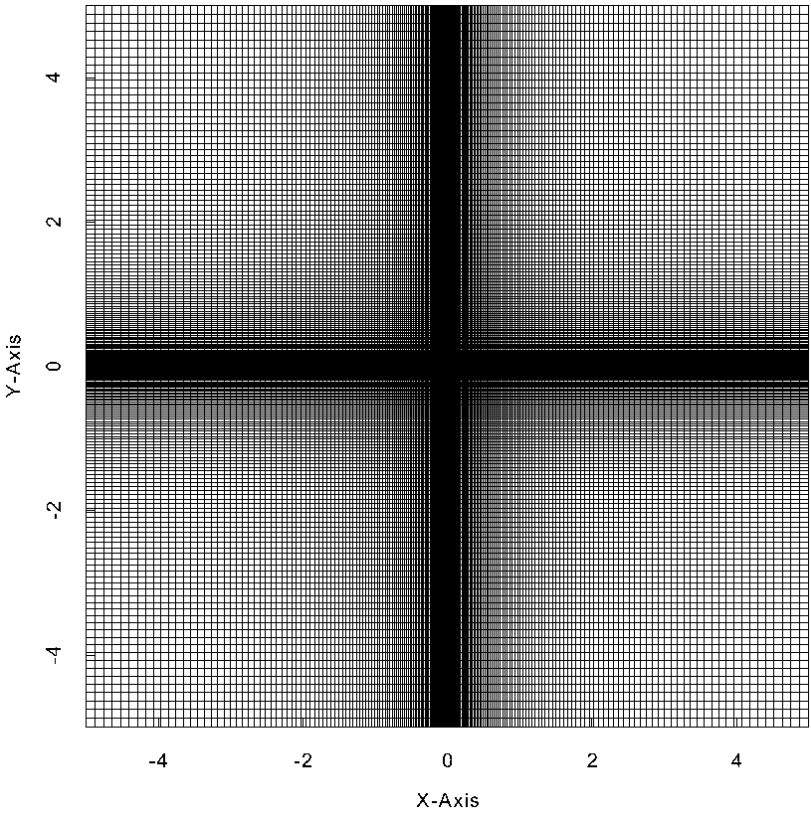

Figure C.1.: Stretched mesh with 100x100 elements

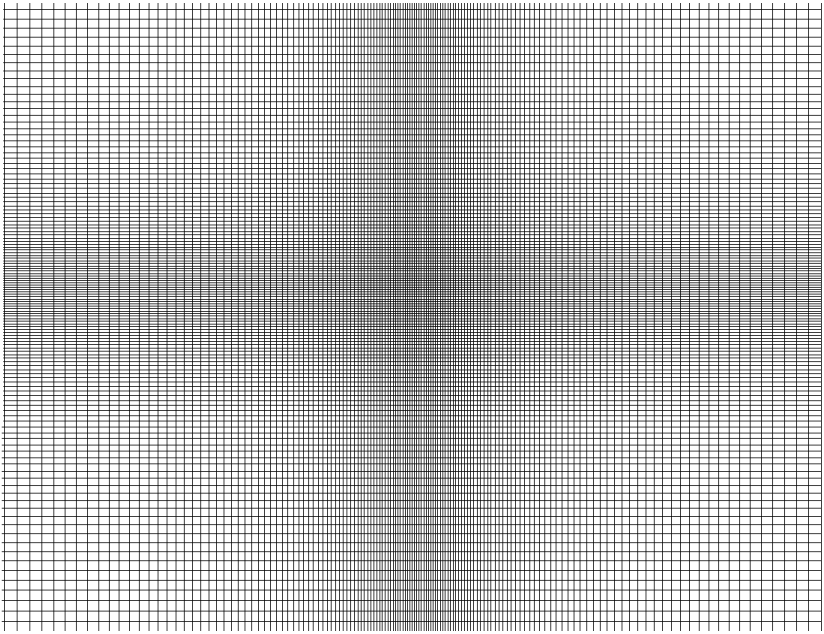

Figure C.2.: Zoom of the stretched mesh with 100x100 elements

Bibliography

[1] The Daedalus Project. *Acta Astronautica*, 49(3–10):555 – 556, 2001.

[2] E. Ahedo and M. Merino. On plasma detachment in propulsive magnetic nozzles. *Physics of Plasmas*, 18(5), 2011.

[3] S. Andersen, V. Jensen, P. Nielsen, and N. D'Angelo. Continuous supersonic plasma wind tunnel. *Physics of Fluids*, 12(3):557–560, 1969.

[4] S. Atzeni and J. M. ter Vehn. *The Physics of Inertial Fusion.* 1st edition, 2009.

[5] P. A. Davidson. *An Introduction to Magnetohydrodynamics.* Cambridge University Press, 1st edition, 2001.

[6] G. A. S. B. D. G. Gaidos, R. A. Lewis and S. Chakrabarti. Antiproton-catalyzed microfission/fusion propulsion systems for exploration of the outer solar system.

[7] X. Guo. An extended hllc riemann solver for the magneto-hydrodynamics including strong internal magnetic field. *Journal of Computational Physics*, 290(0):352 – 363, 2015.

[8] O. A. H. H. S. Park and J. D. Salmonson. High-adiabat high-foot inertial confinement fusion implosion experiments on the national ignition facility. *Physical Review Letters*, 112:52–57, 2014.

[9] A. Hansson. Project Orion: The Atomic Spaceship 1957–1965. *Space Policy*, 19(2):149 – 150, 2003.

[10] F. Hindenlang, G. Gassner, C. Altmann, A. Beck, M. Staudenmaier, and C.-D. Munz. Explicit discontinuous galerkin methods for unsteady problems. *Computers & Fluids*, 61:86–93, 2012.

[11] J. D. Huba. *NRL Plasma Formulary.* Office of Naval Research, 2006.

[12] A. E. Hubbard. Advances in burning plasma-related physics and technology in magnetic fusion. Presentation at the Fusion Energy Symposium 2013.

[13] R. A. Hyde. A laser-fusion rocket for interstellar propulsion. *International Astronautical Federation*, 1983.

[14] K. Ikeda. ITER on the road to fusion energy. *Nucl. Fusion*, 50, 2010.

[15] S. Jardin. *Computational Methods in plasma physics.* CRC Press, 2010.

[16] P. K. Kaw and I. Bandyopadhyay. *Fusion Physics, IAEA 2012*, chapter 1, pages 1–51.

[17] M. Keilhacker and the ASDEX TEAM. The ASDEX divertor tokamak. In *Proceedings of 8th International Conference on Plasma Physics and Controlled Nuclear Fusion Research*, 1980.

[18] R. Kodama. Nuclear fusion: Fast heating scalable to laser fusion ignition. *Nature*, 418:933–934, 2002.

[19] J. D. Lawson. Some criteria for a power producing thermonuclear reactor. *Proc. Phys. Soc. B*, 70, 1957.

[20] R. J. LeVeque. *Finite Volume Methods for Hyperbolic Problems.* Cambridge University Press, 2002.

[21] K. Long, R. Obousy, and A. Hein. Project Icarus: Optimisation of nuclear fusion propulsion for interstellar missions. *Acta Astronautica*, 68(11–12):1820 – 1829, 2011.

[22] C. A. R. M. D. Rayman, T. C. Fraschetti and C. T. Russel. Dawn: A mission in development for exploration of main belt asteroids Vesta and Ceres. *Acta Astronautica*, 58:605–616, 2006.

[23] Y. K. N. Matsuda, A. Maeno and H. Nakashima. A magnetic thrust chamber design for a laser fusion rocket based on impact fast ignition scheme. *Plasma Fusion Res. Series*, 8, 2009.

[24] Y. K. N. Sakaguchi and H. Nakashima. Thrust efficiency calculation for magnetic nozzle in laser fusion rocket. *Trans. Japan Soc. Aero. Space Sci.*, 48(161):180–182, 2005.

[25] Y. Nagamine and H. Nakashima. Analysis of plasma behaviour in a magnetic thrust chamber of a laser fusion rocket. *Fusion Technology*, 35, 1999.

[26] S. Pflanzer. *An introduction to Intertial Confinement Fusion.* Tylor and Francis, 1st edition.

[27] O. Puyoo and L. B. Jaffel. The intrinsic properties of the local interstellar medium. *Lect.Notes Phys.*, 29, 1998.

[28] Y. K. H. N. R. Kawabuchi, N. Matsuda and Y. P. Zakharov. Numerical simulation of plasma detachment from a magnetic nozzle by using fully particle-in-cell code. *Journal of Physics: Conference Series*, 112(4):042082, 2008.

[29] V. Smirnov. Tokamak foundation in ussr/russia 1950-1990. *Nucl. Fusion*, 50, 2010.

[30] G. P. Sutton and O. Biblarz. *Rocket Propulsion Elements.* John Wiley and Sons, Inc., 7th edition.

[31] D. Swanson. Chapter 3 - Waves in fluid plasmas. In D. Swanson, editor, *Plasma Waves*, pages 77 – 118. Academic Press, 1989.

[32] S. K. T. Harada and Y. Kawaguchi. Smoothed Particle Hydrodynamics on GPUs. *The Visual Computer.*

[33] T. M. T. Kawasaki and H. Nakashima. Development of a MHD code using CIP method and its application to a laser fusion rocket. In *26th International Electric Propulsion Conference*, 1999.

[34] E. Toro. *Riemann Solvers and Numerical Methods for Fluid Dynamics.* Springer, June 1999.

[35] K. V. Vchivkov, H. Nakashima, F. Ichikawa, and Y. P. Zakharov. Optimization of thrust efficiency in laser fusion rocket by using three-dimensional hybrid particle-in-cell code. *Vacuum*, 73(3–4):427 – 432, 2004. The 4th International Symposium on Applied Plasma Science.

[36] J. L. T. W. C. Elmore and K. M. Watson. On the Inertial-Electrostatic Confinement of a plasma. *The Physics of Fluids*, 2, 1959.

[37] J. Wesson. *Tokamaks.* Clarendon Press, Oxford, 3rd edition, 2004.

[38] P. J. Wisoff, E. G. V. B. D. F. Bowers, M. W., and D. R. Jedlovec. Nif injection laser system. In *Optical Engineering at the Lawrence Livermore National Laboratory II: The National Ignition Facility*, volume 5341 of *Society of Photo-Optical Instrumentation Engineers (SPIE) Conference Series*, pages 146–155, 2004.

[39] G. A. Wurden. FRX-L: A plasma injector for Magnetized Target Fusion. Physics Division Research Review at Air Force Research Laboratory.

[40] R. K. Y. Kajimura and H. Nakashima. Control techniques of thrust vector for magnetic nozzle in laser fusion rocket. *Fusion Engineering and Design*, 81:2871–2875, 2006.

[41] C. D. Zhou and R. Betti. Hydrodynamic relations for direct-drive fast-ignition and conventional inertial confinement fusion implosions. *Physics of Plasmas*, 14(7), 2007.

List of Tables

List of Figures